UNIVERSITAT DE BARCELONA

MASTER'S THESIS

Master in Quantum Science and Technology

Quantum complexity in high-energy many-body systems

Roger Picañol Narbona

Supervisor: Dr. Paolo Stornati

Barcelona Supercomputing Center

Master in Quantum Science and Technology Barcelona

Barcelona Supercomputing Center
Centro Nacional de Supercomputación

July 2026

Quantum complexity in high-energy many-body systems

Roger Picañol Narbona

Supervised by: Dr. Paolo Stornati

Barcelona Supercomputing Center, 08034 Barcelona
July 2026

The study of quantum many-body systems is a fundamental problem in modern physics, with direct connections to quantum simulation, condensed matter, high-energy physics, and quantum information. A central challenge is to understand which many-body states can be efficiently represented and simulated classically, and which ones require genuinely quantum computational resources. This question is naturally tied to the notion of quantum complexity, which can be probed through diagnostics such as entanglement entropy and non-Gaussianity.

In this thesis, we study complexity markers in interacting fermionic quantum many-body systems. We first analyze a model interpolating between the chaotic Sachdev–Ye–Kitaev (SYK) model and the integrable transverse-field Ising model. Using the half-chain von Neumann entanglement entropy and the fermionic antiflatness, a recently introduced measure of fermionic non-Gaussianity, we characterize the transition between chaotic and integrable regimes in both ground states and excited states. We also discuss symmetry-protected effects in the SYK limit, where antiunitary symmetries can lead to the exact vanishing of the fermionic covariance matrix for specific system sizes.

We then apply these ideas to the lattice Schwinger model, where tensor-network methods are used to study the ground-state phase transition and real-time dynamics. In particular, we investigate how fermionic antiflatness and entanglement behave near criticality, and how their finite-size scaling can be used to extract universal features of the transition. Overall, this thesis shows that fermionic magic and entanglement provide complementary information about the structure and complexity of quantum many-body states.

Keywords: Fermionic non-Gaussianity, Sachdev–Ye–Kitaev model, Quantum phase transitions, Schwinger model, Tensor Networks, Real-time dynamics.

Roger Picañol Narbona: rpicanna7@alumnes.ub.edu

Acknowledgements

This Master's thesis, although written by me, is the result of a collective effort. Firstly, I would like to express my deepest gratitude to my supervisor, Dr. Paolo Stornati, for his scientific guidance, constant support, and kindness throughout this project. His knowledge and advice have been invaluable during the many months we have worked together. I would also like to thank the entire BSC Quantic group for their continuous support and for making the months I spent working on this thesis such an enjoyable experience. Thank you for all the lunches we shared together in the sun. Finally, I would like to thank my parents and closest friends for their unconditional support. This work also belongs to you.

Contents

1 Introduction

Understanding the computational complexity of quantum many-body states is a central challenge in quantum information science, condensed matter, and high-energy physics. Despite the exponential growth of the Hilbert space, many physical systems contain structures that can be used to greatly reduce the cost of processing quantum states. A central question is therefore to determine which quantum states can be simulated efficiently with classical computers and which may have true quantum computational advantages. In order to assess this complexity of quantum states, one can consider entanglement theory, which is a central resource in quantum computation and serves as a powerful diagnostic in many-body physics [WSL04, AFOV08]. For instance, it has been widely used to study quantum phase transitions and thermalization or chaos in physical systems. In this context, it has been established that states with low entanglement can be efficiently representable by Matrix Product States (MPS), which explains the success of the Density Matrix Renormalization Group (DMRG) in one-dimensional systems [Vid03]. In contrast, states with volume-law entanglement, which often appear in out-of-equilibrium systems, cannot be efficiently described using standard Tensor Network (TN) methods.

Nevertheless, entanglement alone is insufficient to fully capture the computational complexity of quantum states. For instance, highly entangled states generated by Clifford circuits, such as Bell states, remain classically simulable [FBFT25]. This motivates the development of the resource theory of non-stabilizerness, often referred to as magic, which quantifies the computational resources needed to describe quantum states beyond stabilizer states and required for universal quantum computation [VMGE14, BSS16]. A prominent measure within this framework is the Stabilizer Rényi Entropy (SRE), which quantifies the non-stabilizerness of quantum states and can be efficiently computed classically [LOH22].

For the fermionic systems considered in this thesis, another natural notion of simplicity is provided by fermionic Gaussian states. These states are generated from the vacuum state by Gaussian unitaries and can be efficiently simulated on classical computers [Val01]. Deviations from Gaussianity, which are commonly referred to as fermionic magic or fermionic non-Gaussianity, play a role analogous to quantum magic, constituting an essential resource for achieving quantum computational advantage. In this work, we employ the Fermionic Antiflatness (FAF), a recently introduced measure inspired by the construction of SRE, which belongs to the resource theory of fermionic non-Gaussianity [SST26]. It vanishes for Gaussian states, remains invariant under Gaussian operations, and increases with the strength of non-Gaussian correlations. This makes it particularly suitable for studying interacting fermionic models relevant to high-energy physics, such as Majorana models and the lattice Schwinger model.

We first consider the Sachdev–Ye–Kitaev (SYK) model coupled to an Ising chain. The SYK model is a prototypical example of a maximally chaotic quantum many-body system [Sac15], originally introduced in the context of non-Fermi liquids, and is also a well-established system in the study of black holes and quantum gravity through the AdS/CFT correspondence [CGAH$^+$17, Wit98]. On the other hand, the Ising limit is integrable and can be mapped to a quadratic fermionic Hamiltonian. The interpolation between these two limits provides a controlled setting to study how FAF changes when going from a chaotic, highly non-Gaussian regime to an integrable free-fermionic one.

Second, we turn to lattice gauge theories (LGTs). Gauge theories constitute the theoretical framework used to describe the fundamental interactions between elementary particles. However, solving interacting gauge theories from first principles is a difficult problem, especially in regimes where perturbative methods can't be used. The paradigmatic

example is quantum chromodynamics (QCD), whose low-energy physics is governed by strong-coupling and non-perturbative effects. LGT, first introduced by Wilson [Wil74], provides a non-perturbative regularization of gauge field theories by formulating them on a discrete spacetime lattice and has become the main tool for studying strongly coupled gauge theories.

A particularly interesting study case is the Schwinger model, which is one-dimensional quantum electrodynamics (1+1D QED) and shares many low-energy phenomena with QCD, such as confinement, chiral symmetry breaking, and nontrivial topological θ vacuum. It is the simplest gauge theory and has been adopted as a benchmark model for lattice methods and, in particular, for TN simulations of gauge theories in $(1+1)$ dimensions. It is therefore a natural setting in which to test whether fermionic complexity markers such as FAF can provide useful information in LGTs.

We study the Schwinger model in two complementary regimes. First, we study its equilibrium phase transition at $\theta = \pi$, where the model undergoes a transition between a CP-symmetric phase and a CP-broken phase. We use FAF to detect this transition and to analyze the scaling of its leading and subleading contributions. Second, we study real-time scattering at vanishing background field, $\theta = 0$, where two vector-meson wave packets collide. This allows us to test whether local versions of FAF can detect the correlations generated during elastic and inelastic scattering processes.

The scattering part of this work is motivated by the fact that collision processes provide one of the most direct probes of subatomic physics. They are essential for verifying the theoretical description of elementary particles and their interactions, as well as for producing high-energy and rare particles. However, their theoretical description is especially challenging when non-perturbative effects that cannot be captured by conventional diagrammatic perturbation theory are important, as in hadronic processes governed by QCD [DHK24].

In order to address these challenges, LGT combined with Quantum Monte Carlo (QMC) has been extremely successful in the study of equilibrium properties, including the hadron spectrum in QCD [DHK24]. However, simulating real-time dynamics remains considerably more challenging, as QMC methods are usually formulated in Euclidean time and suffer from the sign problem when applied directly to real-time evolution, which limits their applicability to dynamical scattering processes. To overcome this limitation, TN methods provide an alternative approach and have been demonstrated to allow for reliable simulations in these regimes in low-dimensional LGTs [CCJ+25, PKBn25]. Their efficiency, however, is limited by the growth of entanglement during time evolution, but they can nevertheless access short and intermediate time scales.

1.1 Complexity markers

Different markers have been introduced to quantify the complexity of quantum states, each probing different aspects of the structure of the wavefunction. This is necessary because there is no unique notion of quantum complexity. For instance, a state may be highly entangled but still efficiently simulable. Consequently, a complete diagnosis of complexity requires comparing several complementary quantities. This section introduces the main markers we will employ that are directly connected to classical simulability and quantum resources: entanglement entropy, SRE and FAF.

First, we will study the von Neumann entanglement entropy with a half-half bipartition of a Hilbert space. We can define it for the bipartition $\mathcal{H} = \mathcal{H}_A \otimes \mathcal{H}_B$, as

$$S(\rho_A) = -\mathrm{Tr}(\rho_A \log_2 \rho_A)\,, \tag{1}$$

where $\rho_A = \mathrm{Tr}_B\left(|\Psi\rangle\langle\Psi|\right)$ is the reduced density matrix. The second complexity marker is the SRE [LOH22]. It captures how a state is distributed when expressed in the basis of Pauli operators $P \in \mathcal{P}_N$, where $\mathcal{P}_N$ represents the Pauli group for N-qubits. The q-th order SRE of a state $|\Psi\rangle$ is defined as

$$\mathcal{M}_q(\Psi) = \frac{1}{1-q}\log_2 \sum_{P\in\mathcal{P}_N} \frac{|\langle\Psi|P|\Psi\rangle|^{2q}}{2^N}, \tag{2}$$

and it quantifies the nonstabilizerness of the state, as previously mentioned. The third marker is the FAF, which can be efficiently computed in large systems with TN techniques and fulfills the properties of a fermionic non-Gaussianity measure: (i) *faithfulness:* $\mathcal{F}_k(|\Psi\rangle) \geq 0$ with equality if and only if the state $|\Psi\rangle$ is fermionic Gaussian; (ii) *invariance under fermionic Gaussian unitaries (FGU):* $\mathcal{F}_k(U_G|\Psi\rangle) = \mathcal{F}_k(|\Psi\rangle)$, where U_G denotes a FGU; (iii) *subadditivity:* $\mathcal{F}_k(|\Psi\rangle\otimes|\Phi\rangle) \leq \mathcal{F}_k(|\Psi\rangle) + \mathcal{F}_k(|\Phi\rangle)$ and *additivity* if at least one of the states $|\Psi\rangle$, $|\Phi\rangle$ has a well-defined fermionic parity, $\mathcal{F}_k(|\Psi\rangle\otimes|\Phi\rangle) = \mathcal{F}_k(|\Psi\rangle)+\mathcal{F}_k(|\Phi\rangle)$ [SST26]. For a pure state $|\Psi\rangle$ of N fermionic modes, it is defined as

$$\mathcal{F}_k(|\Psi\rangle) = N - \frac{1}{2}\,\mathrm{tr}\left[(M^{\mathsf{T}}M)^k\right], \tag{3}$$

where $k \geq 1$ is an integer and M is the $2N \times 2N$ antisymmetric covariance matrix, with matrix elements:

$$M_{mn} = -\frac{i}{2}\langle\Psi|[\gamma_m, \gamma_n]|\Psi\rangle. \tag{4}$$

FAF is thus directly linked to two-point Majorana correlations and complements entanglement and stabilizer-based measures in characterizing the computational complexity of quantum many-body states.

A natural benchmark for assessing the magnitude of the FAF is its typical value for Haar-random pure states, which represents the maximally generic state in Hilbert space [SST26]:

$$\mathcal{F}_1^{\mathrm{typ}} = N - \frac{1}{2^N+1}\,N(2N-1), \tag{5}$$

for $N \geq 2$. These expressions provide a natural reference scale for FAF as states whose antiflatness approaches the Haar-random value are highly complex and strongly non-Gaussian.

Since the FAF is naturally formulated in terms of Majorana correlation matrices, the Jordan-Wigner transformation will play a central role throughout this work [JW28]. This transformation maps Majorana operators onto nonlocal Pauli strings according to

$$\gamma_{2k-1} = \left(\prod_{j=1}^{k-1}\sigma_j^z\right)\sigma_k^x, \qquad \gamma_{2k} = \left(\prod_{j=1}^{k-1}\sigma_j^z\right)\sigma_k^y. \tag{6}$$

The Majorana operators fulfill the anticommutation relations $\{\gamma_i, \gamma_j\} = 2\,\delta_{ij}$ and are traceless and Hermitian $\gamma_i = \gamma_i^\dagger$. For later use in this work, we can define the corresponding standard complex fermions c_n and $c_n^\dagger$, which are related to the Majorana modes through the linear combinations $c_n = (\gamma_{2n-1} - i\gamma_{2n})/2$ and $c_n^\dagger = (\gamma_{2n-1} + i\gamma_{2n})/2$. Substituting Eq. (6) into these definitions yields the Jordan-Wigner mapping for complex fermions:

$$c_n = \left(\prod_{j=1}^{n-1}\sigma_j^z\right)\sigma_n^-, \qquad c_n^\dagger = \left(\prod_{j=1}^{n-1}\sigma_j^z\right)\sigma_n^+, \tag{7}$$

where $\sigma^\pm = (\sigma^x \pm i\sigma^y)/2$.

1.2 Numerical methods

The numerical study of quantum many-body systems is limited by the exponential growth of the Hilbert-space dimension with the number of particles. Consequently, exact diagonalization (ED) becomes computationally intractable for large systems. Nevertheless, for the relatively small system sizes considered in the SYK–Ising model, ED provides direct access to the eigenvalues and eigenstates of the Hamiltonian.

Accessing the larger system sizes required for the lattice Schwinger model therefore calls for a different numerical approach. Although the full Hilbert space is exponentially large, the low-energy states of local Hamiltonians are not generic, highly entangled vectors. Instead, they occupy a tiny, highly structured corner of the Hilbert space [SCS25].

Furthermore, if we bipartition a D-dimensional system into subregions A and B, the "area laws" predict that for ground states of local and gapped Hamiltonians the entanglement entropy $S(\rho_A)$ (defined in Eq. (1)) is not extensive; it scales only with the boundary area of the subregion ($S(\rho_A) \sim L^{D-1}$) [ECP10, LRV04]. Moreover, this implies that for one-dimensional (1D) systems, the entanglement entropy is completely independent of the subsystem size ($S(\rho_A) \sim \text{const}$) [VLRK03].

TN methods exploit this exact physical insight. The efficiency of a TN algorithm is determined by its bond dimension χ, which controls the amount of entanglement present in the system. Because this entanglement is restricted by the area law in 1D gapped ground states, the required bond dimension χ does not grow with the system size. Even for 1D critical systems, the computational cost scales only polynomially [Sch11, Sto22]. This ensures that the computational resources scale favorably with the system size.

MPS provide the efficient parametrization for the states of the relevant corner of the Hilbert space and are built precisely to exploit the low-entanglement structure [SCS25]. For open boundaries and N sites, the ansatz is given by

$$|\Psi\rangle = \sum_{i_0,\ldots,i_{N-1}} M_0^{i_0} \ldots M_{N-1}^{i_{N-1}} |i_0\rangle \otimes \cdots \otimes |i_{N-1}\rangle \,, \tag{8}$$

where $\{|i_k\rangle\}_{k=0}^{d-1}$ is a local basis for the Hilbert space of site k, $M_k^{i_k}$ are complex $\chi \times \chi$ matrices for $0 < k < N-1$, and $M_0^{i_0}$ ($M_{N-1}^{i_{N-1}}$) is a χ-dimensional row (column) vector. The size of these matrices is the previously introduced bond dimension of the MPS χ and determines the number of parameters in the ansatz. Ground states of local one-dimensional Hamiltonians can therefore be represented accurately with moderate bond dimensions, making variational optimization within the MPS manifold highly efficient.

In practice, the Hamiltonian is represented as a Matrix Product Operator (MPO), which provides a TN representation compatible with the MPS ansatz and allows expectation values and operator applications to be evaluated efficiently.

The resulting MPS-MPO framework forms the basis of the DMRG algorithm, which we employ to determine the ground states of systems studied in this work [Whi92]. Instead of addressing the intractable global optimization of the many-body landscape, DMRG frames the search for the ground state as a variational problem, minimizing the energy expectation value $E = \langle\Psi|H|\Psi\rangle / \langle\Psi|\Psi\rangle$ locally.

The algorithm optimizes the MPS ansatz iteratively by sweeping back and forth across the 1D chain. In its standard two-site formulation, DMRG focuses on two neighboring MPS tensors at a time, contracting the rest of the network into effective "left" and "right" environments. This projection reduces the local minimization to a tractable eigenvalue problem. After obtaining the optimal combined two-site tensor, it must be factorized back into two separate tensors using a singular value decomposition (SVD) in order to

restore the MPS form. During this factorization, the entanglement spectrum is truncated up to a maximum bond dimension χ. This preserves the dominant contributions to the decomposition while controlling the computational cost [Sch11].

In the final part of this thesis, we work with real-time dynamics [PDR+16]. For time evolution, we employ the Time-Dependent Variational Principle (TDVP) [HCO+11], which projects the Schrödinger dynamics onto the tangent space of the MPS manifold. Unlike Trotter-based approaches, which approximate the time-evolution operator through a Suzuki–Trotter decomposition into local gates, TDVP evolves the state directly within the MPS variational manifold. The time-evolved state is optimally approximated at each time step with a maximum bond dimension χ, remaining within the restricted set of low-entanglement states.

The remainder of this work is organized into two main parts. First, we will study the crossover from a chaotic to an integrable phase and whether it is accompanied by an abrupt change in the system's complexity. Next, we will analyze the CP-symmetry breaking phase transition in the lattice Schwinger model and investigate the out-of-equilibrium dynamics of the Schwinger model by evaluating the collision of two fermionic wave packets.

2 Chaotic–integrable transition in the SYK model

As introduced above, we first study a model interpolating between a chaotic SYK_4 Hamiltonian and an integrable Ising chain. The system is composed of M interacting Majorana fermions, corresponding to $N = M/2$ qubits, and is defined by

$$H = (1-\lambda)H_{\mathrm{SYK}_4} + \lambda H_{\mathrm{Ising}}. \tag{8}$$

The parameter λ controls the interpolation between the chaotic limit, $\lambda = 0$, and the integrable limit, $\lambda = 1$. The SYK_q Hamiltonian describes M Majorana fermions with random all-to-all q-body interactions,

$$H_{\mathrm{SYK}_q} = (i)^{q/2} \sum_{1\le i_1<\cdots<i_q\le M} J_{i_1\cdots i_q}\gamma_{i_1}\cdots\gamma_{i_q}, \tag{9}$$

where the couplings $J_{i_1\cdots i_q}$ are independent Gaussian random variables with zero mean and variance

$$\left\langle J^2_{i_1\cdots i_q}\right\rangle = \frac{J^2(q-1)!}{M^{q-1}}. \tag{10}$$

In this work we focus on the case $q = 4$. The integrable limit is the transverse-field Ising model (TFIM),

$$H_{\mathrm{Ising}} = -J\sum_{i=1}^{N-1}\sigma_i^x\sigma_{i+1}^x - h\sum_{i=1}^{N}\sigma_i^z, \tag{11}$$

where h and J are parameters of the model and are set to $J = h = 1$ to fix the energy scale. We can convert the Pauli operators acting on the i-th qubit onto Majorana operators using the Jordan-Wigner transformations previously defined in Eq. (6). Then, the Ising Hamiltonian in terms of these operators is written as

$$H_{\mathrm{Ising}} = iJ\sum_{i=1}^{N-1}\gamma_{2i}\gamma_{2i+1} + ih\sum_{i=1}^{N}\gamma_{2i-1}\gamma_{2i}, \tag{12}$$

featuring only quadratic interactions between the Majorana modes. Thus, increasing λ gradually replaces the random all-to-all four-body interactions of the SYK_4 model by a local quadratic Majorana Hamiltonian.

Finally, the symmetries of our model are crucial for correctly defining and interpreting the complexity markers. Both Hamiltonians commute with the fermion parity operator $\mathcal{P}$ and thus the full Hamiltonian H is block-diagonal. The SYK_4 model also commutes with the anti-unitary operator $\mathcal{T}$, whereas the Ising term anticommutes with it. This interplay between $\mathcal{P}$ and $\mathcal{T}$ determines the Random Matrix Theory (RMT) ensemble and degeneracy of the ground state of the SYK_4 model: for $N \equiv 2 \pmod 4$ the ensemble corresponds to Gaussian Symplectic Ensemble (GSE), for $N \equiv 0 \pmod 4$ the corresponding ensemble is Gaussian Orthogonal Ensemble (GOE), and for $N \equiv 1, 3 \pmod 4$ it is the Gaussian Unitary Ensemble (GUE) [SWB+25]. These classes lead to distinct finite-size behavior of the complexity markers. Introducing the Ising perturbation ($\lambda > 0$) immediately breaks the antiunitary symmetry of the full Hamiltonian and alters the underlying RMT class of the system during the transition.

2.1 Ground-state complexity across the crossover

We first characterize the ground-state properties across the crossover by analyzing the behavior of some of the complexity markers introduced above: the entanglement entropy density, S/N, and the FAF density, $\mathcal{F}_1/N$. To account for the disorder in the SYK_4 contribution, the results are averaged over an ensemble of random realizations. For each value of λ and each disorder realization, the ground state is obtained by ED and the two complexity markers are evaluated from the corresponding eigenvector. A detailed summary of the number of disorder realizations can be found in Appendix A.

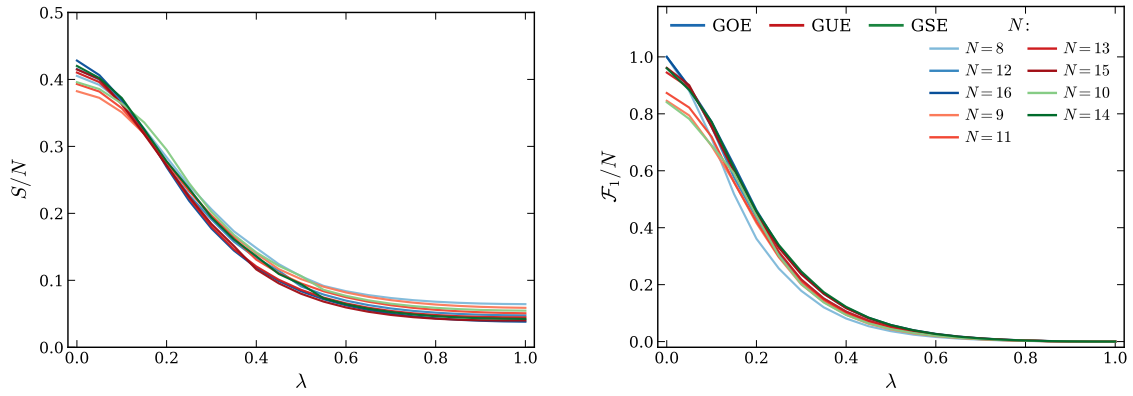

Figure 1: Disorder-averaged entropy density S/N and FAF density $\mathcal{F}_1/N$ as a function of the interpolation parameter λ for the ground state of the Hamiltonian in Eq. (8). The curves are colored according to the RMT class of the corresponding pure-SYK_4 limit: GOE, GUE, or GSE.

As shown in Fig. 1, both the entanglement entropy density S/N and the FAF density $\mathcal{F}_1/N$ decrease as the interpolation parameter λ is increased from the chaotic SYK_4 limit towards the integrable Ising limit. The entropy density approaches the expected Haar-random values for $\lambda \to 0$ (the purely chaotic SYK_4 limit)[SWB+25], and towards the integrable Ising limit, it decreases with increasing system size. In our case, $J = h = 1$ places the TFIM at its critical point, where the half-chain entanglement entropy is expected to grow logarithmically with N. Consequently, the entropy density vanishes asymptotically as $S/N \sim (\ln N)/N$.

Regarding the FAF, its behavior strongly reflects the non-Gaussianity of the states. It is precisely zero in the Ising model ($\lambda = 1$), as theoretically expected. This is because the ground state of the TFIM is a fermionic Gaussian state and thus it contains no fermionic magic resources, $\mathcal{F}_k(|\Psi_0\rangle) = 0$. In contrast, close to the SYK_4 limit, the FAF does not

trivially saturate the Haar-random values in the same manner as the entropy and displays a clear dependence on the system size and on the symmetry class of the model. Specifically, for $N \equiv 0 \pmod 4$, the Majorana covariance matrix vanishes and FAF yields $\mathcal{F}_k/N = 1$. This modular periodicity, which holds for both ground and excited states, is relevant and will be analyzed in detail. The qualitative behavior of FAF for $k = 1$ and $k = 2$ is nearly the same, as shown in Appendix B.

Finally, one can also observe that the two markers deviate from their ergodic values as λ moves away from $\lambda \sim 0$, indicating that the SYK_4 ground state is highly sensitive to perturbations from the Ising contribution. In contrast, both complexity markers approach their values of $\lambda \sim 1$ for $\lambda \gtrsim 0.5$ with no significant variation and exhibit a broad plateau, smoothly approaching their asymptotic values at $\lambda = 1$. Overall, this analysis suggests that no single marker can independently describe all relevant regimes of the system, and that the FAF density exhibits a much richer structure and is significantly more sensitive to the underlying symmetries of the system.

2.2 FAF across the energy spectrum

We now extend the analysis from the ground state to excited states. For this purpose, Fig. 2 shows the ED results for $\mathcal{F}_1$ across the energy spectrum E for several values of λ. The mean behavior is highlighted by the solid darker line in panels (a) and (b), while the theoretical typical value $\mathcal{F}_1^{\mathrm{typ}}$, defined in Eq. (5), is superimposed using dashed lines for different system sizes N. In panels (c) and (d), the data are shown without the average curves in order to display more clearly the flattening of the spectral profile and its symmetry-dependent structure in the SYK_4 limit. All results are averaged over disorder realizations, whose number for each system size is reported in Appendix A.

The quantum Ising limit ($\lambda = 1$) has been omitted from the graphical representation. The reason is that, as discussed earlier for the ground state, the FAF vanishes identically ($\mathcal{F}_1 = 0$) across the entire energy spectrum. This is because the 1D quantum Ising model maps to an integrable quadratic fermionic system and thus the FAF yields exactly zero for any of its eigenstates, as they are Gaussian states.

As shown in Fig. 2, for the transition phase ($0.2 \lesssim \lambda \lesssim 0.8$), the FAF is suppressed at the edges of the spectrum, near the ground state and the highest excited state, and increases toward the center of the spectrum, where the density of states is maximal. In particular, it is also evident that for $\lambda = 0.75$ the FAF exhibits a pronounced spread between neighboring eigenstates across the entire spectrum, which in the context of the Eigenstate Thermalization Hypothesis (ETH) indicates non-ergodic behavior [Sre94].

As λ is reduced, the mean profile gradually loses its pronounced inverted-parabola shape and becomes progressively flatter. For $\lambda = 0.25$, most mid-spectrum eigenstates are concentrated close to the typical Haar-random reference value, forming a broad plateau across the bulk of the spectrum. This evolution is consistent with the system approaching the ergodic SYK_4 regime, where highly excited eigenstates are expected to exhibit nearly maximal FAF [SST26].

Finally, the purely chaotic case, $\lambda = 0$, reveals a strong dependence on the system size modulo 4. For the accessible system sizes where $N \not\equiv 0 \pmod 4$, the average mid-spectrum FAF approaches the typical Haar-random value. In contrast, for $N = 12$, the Majorana covariance matrix vanishes as a consequence of the antiunitary symmetry, and all eigenstates satisfy $\mathcal{F}_1 = N = 12$.

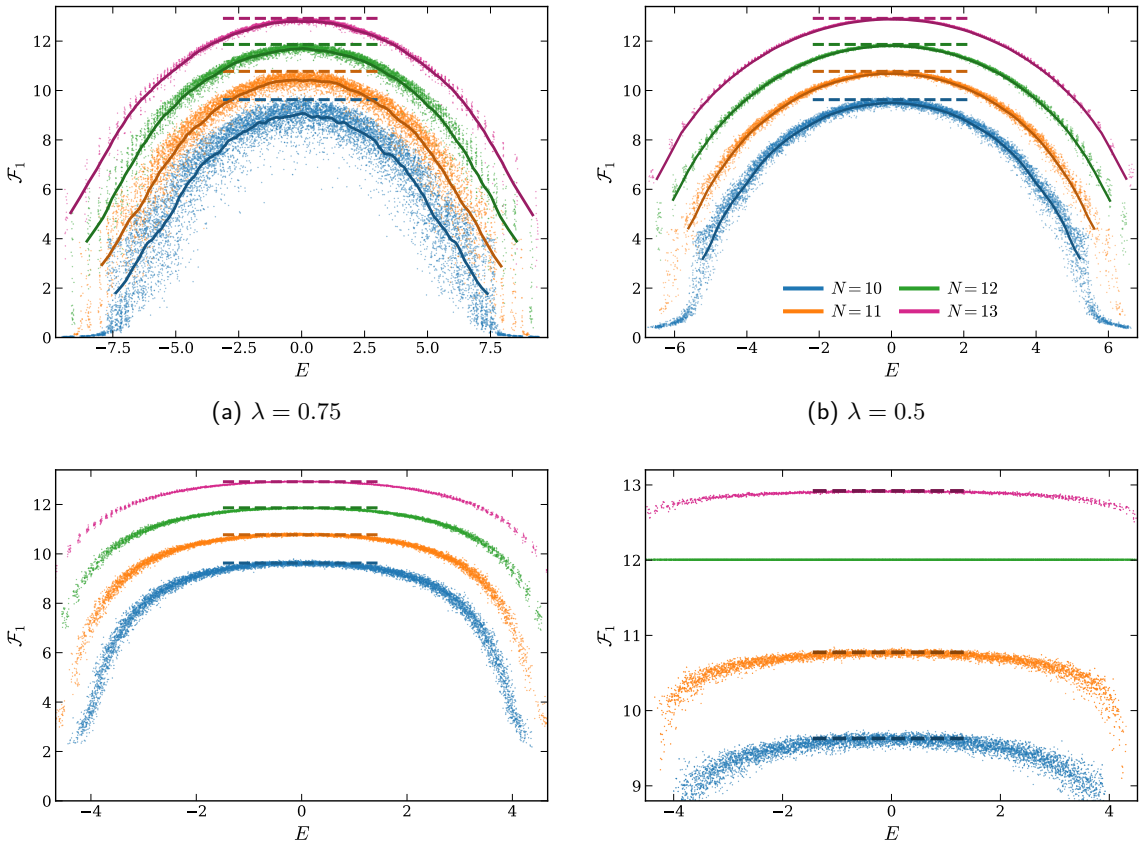

(a) $\lambda = 0.75$ (b) $\lambda = 0.5$

(c) $\lambda = 0.25$ (d) SYK$_4$ model ($\lambda = 0$)

Figure 2: FAF $\mathcal{F}_1$ across the energy spectrum for different values of the interpolation parameter λ and system sizes N. The horizontal dashed lines indicate the typical Haar-random value $\mathcal{F}_1^{\text{typ}}$ for each system size N. **(a)-(c)** Intermediate regimes showing the deformation of the typical state profile. As λ decreases, the inverted-parabola profile progressively develops into a broad plateau across the middle of the spectrum. **(d)** The purely chaotic SYK$_4$ model, where the behavior depends strongly on the finite-N symmetry class. In particular, for $N = 12$, the FAF collapses to a constant value $\mathcal{F}_1 = 12$ across the entire spectrum.

2.3 Finite-size scaling and symmetry classes

To quantify these observations in the pure SYK$_4$ limit and determine how the bulk behavior evolves with system size, we select the min $\left\{1000, \frac{2^N}{20}\right\}$ eigenstates with energies closest to the center of the spectrum, $E = 0$, and compute their mean FAF, $\overline{\mathcal{F}}_1$. We then compare this mean value with the typical Haar-random value $\mathcal{F}_1^{\text{typ}}$. For ergodic systems satisfying ETH, one expects the middle-spectrum eigenstates to become increasingly close to typical states in the large-N limit. In terms of the FAF, this implies that the difference between the mid-spectrum average and the Haar-random value should be suppressed with the system size,

$$\mathcal{F}_1^{\text{typ}} - \overline{\mathcal{F}}_1 \propto N^{-\beta}. \tag{13}$$

Our results are shown in Fig. 3. Overall, the deviation from the Haar-random value decreases as the system size increases. However, the convergence is not uniform across all system sizes. Instead, the data show a clear dependence on the symmetry class, organized according to N mod 4. In particular, the class $N \equiv 0 \pmod 4$ behaves differently from

the others, since the difference $\mathcal{F}_1^{\mathrm{typ}} - \overline{\mathcal{F}}_1$ becomes negative for the accessible system sizes. This shows that the finite-size behavior is affected not only by the Hilbert-space dimension, but also by the symmetry structure of the finite-N SYK_4 Hamiltonian.

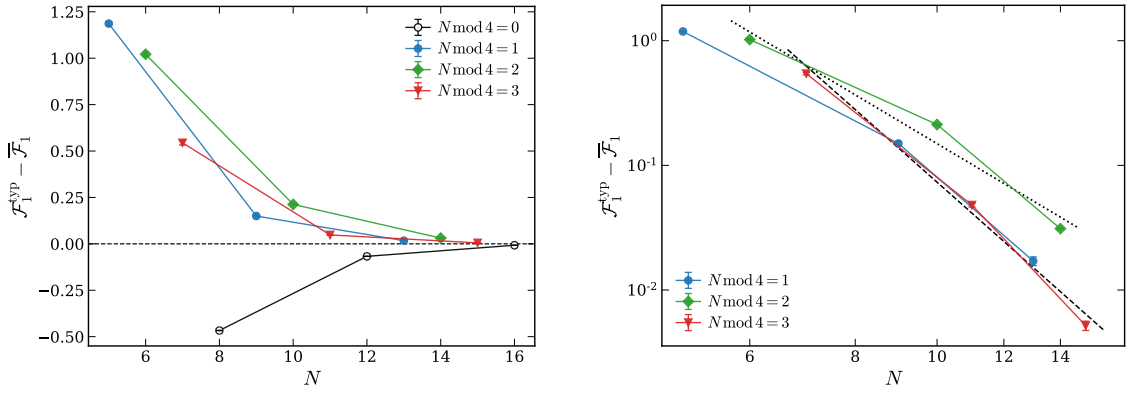

Figure 3: Difference between the typical Haar-random value $\mathcal{F}_1^{\mathrm{typ}}$ and the mean mid-spectrum FAF $\overline{\mathcal{F}}_1$ as a function of the system size N, separated according to $N \bmod 4$. The left panel shows all symmetry classes, while the right panel includes only the positive deviations and the power-law fits $\mathcal{F}_1^{\mathrm{typ}} - \overline{\mathcal{F}}_1 \propto N^{-\beta}$, yielding $\beta = 6.0(3)$ for $N \equiv 1, 3 \pmod 4$ and $\beta = 4.0(7)$ for $N \equiv 2 \pmod 4$. The deviations decrease overall with increasing N, but the behavior depends strongly on the symmetry class. Because only a limited number of system sizes and disorder realizations are available, the data do not allow for a reliable statistical extraction of the exponent β; the number of realizations underlying each system size is reported in Appendix A.

For the remaining symmetry classes, the positive deviations are shown in the right panel of Fig. 3. Their decrease with N is consistent with convergence towards the Haar-random prediction. Nevertheless, the distinct trends followed by the different $N \bmod 4$ classes show that the convergence retains a strong dependence on the symmetry class of the SYK_4 model.

All in all, the results above show that the behavior of the FAF is not only controlled by the interpolation parameter λ, but also depends strongly on the system size. This can be understood from the definition of the Majorana covariance matrix M_{mn}, Eq. (4), which vanishes identically for eigenstates of the SYK model with $q = 4$ and $N = 8, 12, 16$, while it does not vanish for the other values of N presented. Since the Majorana operators satisfy a Clifford algebra, for $m \neq n$, the commutator reduces to $[\gamma_m, \gamma_n] = 2\gamma_m\gamma_n$. The covariance matrix can then be written as $M_{mn} = -i\langle\Psi|\gamma_m\gamma_n|\Psi\rangle$ for $m \neq n$. Thus, the vanishing of M can be understood by examining how the Majorana bilinears transform under the antiunitary symmetry of the SYK_4 Hamiltonian.

The action of this antiunitary symmetry depends on the representation of the Clifford algebra generated by the M Majorana operators, which exhibits an eightfold periodicity in $M \bmod 8$ [GGV16, LLXZ17, CGAH+17]. Since our system contains $M = 2N$ Majorana modes, this periodicity is equivalently expressed as a dependence on $N \bmod 4$. As discussed above, for $N \equiv 0 \pmod 4$, the SYK_4 Hamiltonian belongs to the GOE class. In this class, the anti-unitary symmetry $\mathcal{T}$ acts within each fixed fermion-parity sector and satisfies

$$[H_{\mathrm{SYK}_4}, \mathcal{T}] = 0, \qquad \mathcal{T}^2 = +1. \tag{14}$$

Therefore, there is no symmetry-protected Kramers degeneracy, and a nondegenerate eigenstate can be chosen to be invariant under $\mathcal{T}$ up to a phase,

$$\mathcal{T}|\Psi\rangle = e^{i\phi}|\Psi\rangle. \tag{15}$$

Under this antiunitary symmetry, the Majorana operators transform as

$$\mathcal{T}\gamma_m\mathcal{T}^{-1} = \eta\gamma_m \quad \text{for } m = 1, \ldots, 2N, \tag{16}$$

where $\eta = \pm 1$ is a global sign that depends on the number of fermions. Since $\mathcal{T}$ is antiunitary, it conjugates the imaginary unit. Therefore, the bilinear operator $O_{mn} = -i\gamma_m\gamma_n$ transforms as

$$\mathcal{T}O_{mn}\mathcal{T}^{-1} = -\eta^2 O_{mn} = -O_{mn}, \tag{17}$$

where we used $\eta^2 = 1$, and it cancels out completely. This shows that O_{mn} is strictly odd under the antiunitary symmetry.

Then, for any operator O that is odd under $\mathcal{T}$, we can evaluate its expectation value by making use of an identity for antiunitary operators, $\langle \mathcal{T}\alpha|\mathcal{T}\beta\rangle = \langle\alpha|\beta\rangle^*$. We have:

$$\langle\Psi|O|\Psi\rangle^* = \langle\mathcal{T}\Psi|\mathcal{T}O|\Psi\rangle = \langle\mathcal{T}\Psi|\mathcal{T}O\mathcal{T}^{-1}\mathcal{T}|\Psi\rangle = \langle\Psi|(-O)|\Psi\rangle$$

where we used that $\mathcal{T}|\Psi\rangle = e^{i\phi}|\Psi\rangle$. Since O is a Hermitian operator, as $\gamma_m\gamma_n$ is anti-Hermitian for $m \neq n$, its expectation value is real, $\langle O\rangle = \langle O\rangle^*$. Hence,

$$\langle\Psi|O|\Psi\rangle = 0. \tag{18}$$

Applying this to $O_{mn} = -i\gamma_m\gamma_n$, we obtain $\langle\Psi| - i\gamma_m\gamma_n|\Psi\rangle = 0$, and therefore

$$M_{mn} = 0. \tag{19}$$

All in all, the vanishing of the covariance matrix M for $N \equiv 0 \pmod 4$ has a direct impact on the characterization of the system's non-Gaussianity, setting the fermionic antiflatness $\mathcal{F}_k(|\Psi\rangle) = N$ for this class.

For the other symmetry classes, the same argument does not apply. When $N \equiv 1, 3 \pmod 4$, the Hamiltonian belongs to the GUE class, and no such antiunitary symmetry exists within a fixed parity block. For $N \equiv 2 \pmod 4$, the system belongs to the GSE class and satisfies $\mathcal{T}^2 = -1$, giving rise to Kramers degeneracy. In this case, an individual eigenstate cannot then be chosen invariant under $\mathcal{T}$, and the bilinear expectation values are not forced to vanish [CGAH+17].

Additionally, for $0 < \lambda < 1$, the symmetry class of our system is lifted to GUE for all N due to the presence of the Ising Hamiltonian, which anticommutes with the antiunitary operator.

3 The lattice Schwinger model

We now turn to the previously introduced lattice Schwinger model. To study this model numerically, we work with the discretized Hamiltonian of the massive Schwinger model on an open chain of N sites (where N is even), using the Kogut-Susskind staggered lattice formulation to avoid the fermion doubling problem [KS75, BSK76]. In this approach, the two components of the Dirac spinor are alternatingly distributed across adjacent lattice sites. The lattice Hamiltonian for 1 flavor with a coupling constant g then reads:

$$\begin{aligned} H_{\mathrm{S}} =& \frac{g^2 a}{2}\sum_{n=0}^{N-2}\left(L_n + \frac{\theta}{2\pi}\right)^2 + m\sum_{n=0}^{N-1}(-1)^n c_n^\dagger c_n \\ & - \frac{i}{2a}\sum_{n=0}^{N-2}\left(c_n^\dagger e^{i\phi_n} c_{n+1} - c_{n+1}^\dagger e^{-i\phi_n} c_n\right), \end{aligned}$$

where a is the lattice spacing, and c_n and $c_n^\dagger$ are the fermion annihilation and creation operators at site n. The operators L_n and ϕ_n act on the gauge links between neighboring fermionic sites, with L_n representing the electric flux on link n. They are canonically conjugate, $[\phi_n, L_m] = i\delta_{nm}$, so that $e^{i\phi_n}$ acts as a raising operator for the electric flux. The parameter θ is the topological vacuum angle, and is set to $\theta = \pi$ on this section. It is related to the background electric field as

$$l = \frac{\theta}{2\pi}.$$

Physical states have to satisfy the Gauss law, $G_n|\Psi\rangle = 0 \quad \forall n$, where

$$G_n = L_n - L_{n-1} - Q_n,$$

and $Q_n = c_n^\dagger c_n - \frac{1}{2}(1 - (-1)^n)$ is the dynamical charge. Therefore, in an open chain, Gauss's law can completely fix the gauge field degrees of freedom in terms of the fermionic charge and the electric flux on any link is then fully determined by the fermionic operators:

$$L_n = \sum_{k=0}^{n} Q_k + L_{\text{in}}\,, \tag{20}$$

where L_{in} is the incoming electric flux from the left of the chain and is set to zero $L_{\text{in}} = 0$. The link variables $e^{i\phi_n}$ can then be eliminated from the kinetic term.

To solve the system using TN methods, we map the complex fermionic operators to a spin-1/2 chain. We achieve this by employing the Jordan-Wigner transformation previously defined in Eq. (7). Applying this transformation, the system is mapped into the dimensionless spin Hamiltonian $W = \frac{2}{g^2 a} H_{\text{S}}$ [BSBH02], given by:

$$W = x \sum_{n=0}^{N-2} \left(\sigma_n^+ \sigma_{n+1}^- + \text{h.c.}\right) + \frac{\mu}{2} \sum_{n=0}^{N-1} (-1)^n \sigma_n^z + \sum_{n=0}^{N-2} \left(L_n + \frac{\theta}{2\pi}\right)^2, \tag{21}$$

where the electric flux is now

$$L_n = \frac{1}{2} \sum_{k=0}^{n} (\sigma_k^z + (-1)^k).$$

Here, we have introduced the dimensionless parameters $x = 1/(g^2a^2)$ and $\mu = 2m/(g^2a)$. The point $\theta = \pi$ is special because the Schwinger model is invariant under CP at this value of the vacuum angle. At zero temperature, increasing the dimensionless fermion mass m/g drives a second-order quantum phase transition from a CP-symmetric phase to a phase in which CP is spontaneously broken. This critical point belongs to the two-dimensional Ising universality class, as seen in [Oha23, BSBH02]. In the continuum limit, the critical point has been accurately located at $m_c/g = 0.333561(4)$ [ACTX25]. The corresponding critical exponents are consistent with the Ising values $\nu = 1$ and $\beta = 1/8$. Due to the lattice formulation, recovering the continuum physical critical mass requires taking the limit $x \to \infty$ (which corresponds to $a \to 0$).

3.1 Ground-state phase transition at $\theta = \pi$

To compute the ground state of the Hamiltonian in Eq. (21), we perform finite-system DMRG sweeps with Open Boundary Conditions (OBC). We also work strictly in the subspace of states satisfying Gauss's law. In our TN implementation, this is enforced by

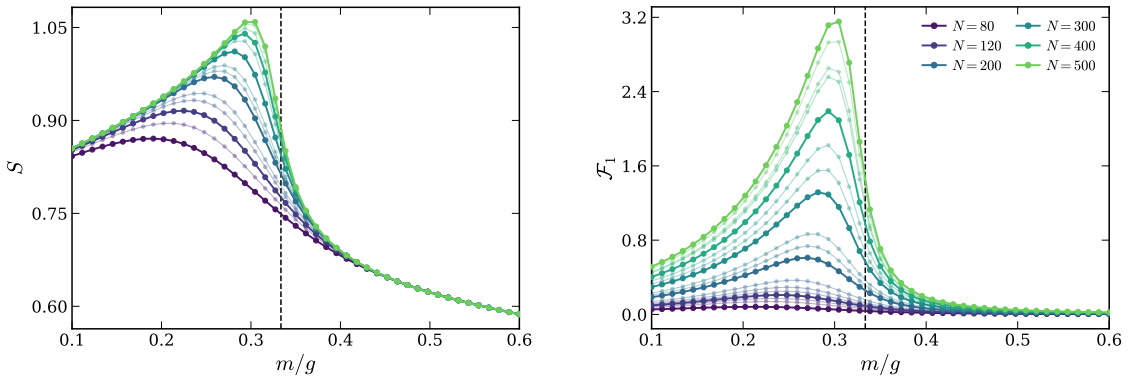

Figure 4: Behavior of the complexity markers across the Schwinger model phase transition. **(Left)** Entanglement entropy S and **(Right)** FAF $\mathcal{F}_1$ as a function of the mass parameter m/g for the ground state. The different curves correspond to varying system sizes ranging from $N = 80$ to $N = 500$. The vertical dashed line at $m_c/g \approx 0.3335$ indicates the expected continuum critical value.

conserving the $U(1)$ total fermion number across the lattice. Once the ground state MPS is converged, we utilize it to characterize the phase transition by measuring the bipartite Entanglement Entropy (Eq. (1)) and probing the non-Gaussianity of the state via the FAF (Eq. (3)).

Fig. 4 shows that both FAF and entropy are enhanced in the vicinity of the transition, $m/g = m_c/g$, and they decrease smoothly away from the critical point, a typical feature of a phase transition. Both observables exhibit clear finite-lattice and finite-size effects, which are significantly stronger around the critical point. This is reflected in the dependence of the position and height of the peaks of the entropy and FAF on the volume. In the thermodynamic and continuum limits, the maxima are expected to approach the critical value $m_c/g \simeq 0.3335$, as mentioned before. Since the present results are obtained at fixed lattice spacing, $x = 40$, it would be required to extrapolate in both volume and lattice spacing to fully characterize the continuum critical behavior.

3.2 Critical scaling of FAF

As introduced in [SST26], due to the additivity of FAF for product states with fixed fermionic parity $\mathcal{P}$, $\mathcal{F}_k$ may scale extensively with the system size N. This suggests the following generic linear scaling of FAF with the system size

$$\mathcal{F}_k = D_k N + f_k, \tag{22}$$

with D_k and f_k the corresponding leading and subleading terms. Since these quantities can depend non-trivially on N, we estimate them locally using two nearby sizes N_1 and $N_2 = N_1 + \Delta N$, with $\Delta N < N_1/8$ [SST26]. Solving Eq. (22) for the two sizes gives

$$D_k = \frac{\mathcal{F}_k(N_2) - \mathcal{F}_k(N_1)}{\Delta N}; \qquad f_k = \frac{N_2\mathcal{F}_k(N_1) - N_1\mathcal{F}_k(N_2)}{\Delta N}.$$

In Fig. 5 we plot the leading and subleading terms D_k and f_k for $k = 1$ as a function of m/g, using the method described above. The shape of $D_1(m/g)$ resembles the behavior of the total FAF qualitatively and develops a maximum near the transition. By contrast, the subleading term f_1 exhibits a much sharper minimum. Importantly, the position of the critical point is better extrapolated from this subleading term instead of the maxima of FAF or D_1. A similar behavior was observed in the Axial Next-Nearest-Neighbor Ising

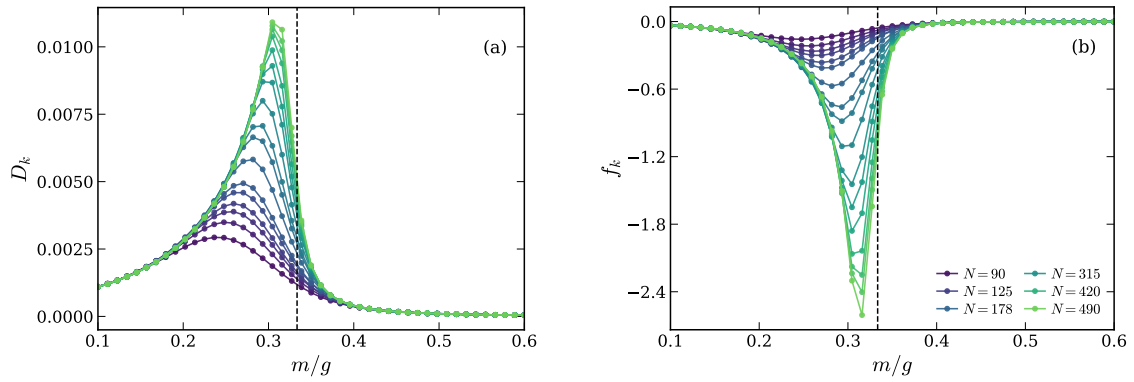

Figure 5: Leading and subleading components of the FAF across the Schwinger model phase transition. **(a)** The extensive leading term D_1 and **(b)** the subleading term f_1 extracted from $\mathcal{F}_1$ as a function of m/g. Each curve is associated with an effective system size $N_{\text{eff}} = (N_1 + N_2)/2$, corresponding to a pair of nearby system sizes. The values range from 90 to 490. Qualitatively, D_1 follows the behavior of $\mathcal{F}_1$ with a maximum near the transition, whereas f_1 exhibits a sharp minimum. The vertical dashed line indicates the critical point.

(ANNNI) model in [SST26]. However, since the present calculations are performed at the fixed lattice parameter $x = 40$, these curves do not yet reflect the continuum limit. Consequently, the minimum of f_1 at large N approaches an effective critical point for this specific lattice spacing, which remains slightly shifted from the exact theoretical continuum value. In our calculations, the large-N extrapolation gives $(m_c/g)_{x=40} \simeq 0.327$.

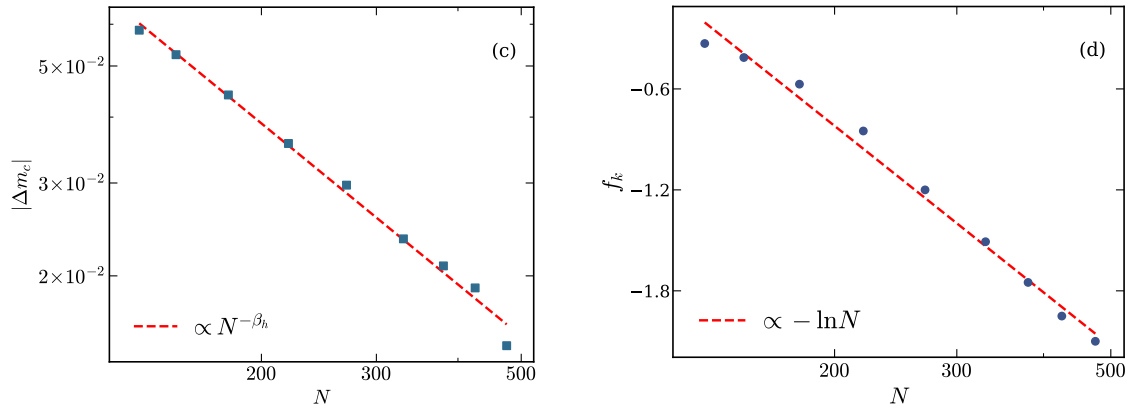

Figure 6: Finite-size scaling analysis at the phase transition. **(c)** Convergence of the pseudocritical point $m_{\min}/g$ towards the effective critical point $(m_c/g)_{x=40}$. The plotted quantity is $\Delta m_c = |m_{\min}/g - (m_c/g)_{x=40}|$ as a function of the effective N. The dashed line corresponds to a power-law fit, $\Delta m_c \propto N^{-\beta_h}$, with $\beta_h = 1.01(3)$. **(d)** Scaling of the minimum value of the subleading term f_1 as a function of the effective system size N. The data are compatible with a logarithmic divergence, $\min(f_1) \propto -\ln N$.

The transition of the massive Schwinger model at $\theta = \pi$ is expected to belong to the Ising universality class, characterized by the critical exponent $\nu = 1$. We use this known result as a reference to analyze the finite-size behavior of the pseudocritical point extracted from the minimum of f_1. In Fig. 6(c), we plot

$$\Delta m_c = \left| \frac{m_{\min}}{g} - \left(\frac{m_c}{g} \right)_{x=40} \right|$$

as a function of the effective system size N. Here, $m_{\min}/g$ denotes the position of the

minimum of f_1. For a continuous transition, the shift is expected to scale as

$$\Delta m_c \propto N^{-1/\nu}. \tag{23}$$

Since $\nu = 1$ for the Ising universality class, the expected behavior is $\Delta m_c \propto N^{-1}$. The fitted exponent $\beta_h = 1.01(3)$ is therefore consistent with the expected Ising scaling. A second analysis is shown in Fig. 6(d). The minimum of the subleading term becomes increasingly negative with the system size, $\min_{m/g} f_1 \propto -\ln N$, and is well described by

$$f_1 = a_1 \ln N + c_1, \tag{24}$$

near the critical region. Here, a_1 is the prefactor of the logarithmic correction ($a_1 < 0$), whereas c_1 is a non-universal constant contribution. The extensive coefficient D_1 is also not expected to be universal.

The ANNNI model studied in [SST26] provides a natural benchmark for these results, since the transition considered there is also described by Ising criticality and the FAF was analyzed under OBC. In both models, the pseudocritical point approaches its thermodynamic value approximately as N^{-1}, while the minimum of the subleading FAF contribution decreases logarithmically with N. Moreover, the fitted logarithmic coefficients are in both cases close to

$$a_1 \simeq -1.$$

The agreement between the two models suggests that this logarithmic correction may be related to their common critical and boundary properties. However, it is not sufficient by itself to establish the universality of the coefficient a_1.

The origin of this logarithmic correction can be understood by rewriting Eq. (3) for $k = 1$ in terms of two-point Majorana correlation functions, as originally observed in [SST26]:

$$\mathcal{F}_1(|\Psi_0\rangle) = N - \frac{1}{2}\sum_i \sum_{j\neq i} |\langle\Psi_0|\gamma_i\gamma_j|\Psi_0\rangle|^2. \tag{25}$$

Away from criticality, these correlations decay exponentially, $\langle\gamma_i\gamma_{i+r}\rangle \sim e^{-r/\xi}$, with a finite correlation length ξ. Close to the critical point, the correlation length diverges as $\xi \sim |\Delta m_c|^{-\nu}$. However, strictly at the critical point, the continuum theory is described by the 1+1-dimensional Ising Conformal Field Theory (CFT), where the Majorana fields have a scaling dimension of $\Delta = 1/2$. The correlator then decays algebraically as $\langle\gamma_i\gamma_{i+r}\rangle \propto 1/r$.

Under OBC, translational invariance is broken by the edges of the chain and $\langle\gamma_i\gamma_{i+r}\rangle$ depends on both i and r. However, one can separate the contributions of the sum $\sum_{j\neq i} |\langle\Psi_0|\gamma_i\gamma_j|\Psi_0\rangle|^2$ in Eq. (25) into a constant bulk contribution s_{bulk} per Majorana mode (which assumes effective translational invariance) and a boundary correction δs_i, which decays as the site i moves deeper into the bulk. Consequently, the FAF can be decomposed as:

$$\mathcal{F}_1(|\Psi_0\rangle) = N\,(1 - s_{\text{bulk}}) - \frac{1}{2}\sum_{i=1}^{2N} \delta s_i, \tag{26}$$

where the first term scales extensively, yielding the leading coefficient $D_1 = 1 - s_{\text{bulk}}$. The sum over the effective boundary corrections δs_i generates the subleading term f_1. Because these corrections reflect the critical power-law behavior of the CFT, they are expected to decay algebraically from the edges: $\delta s_i \propto \max\{1/i, 1/(2N-i)\}$. Summing these corrections over the chain asymptotically gives the logarithmic divergence:

$$f_1 = -\frac{1}{2}\sum_{i=1}^{2N} \delta s_i \propto a_1 \ln N + c_1.$$

This provides a possible explanation for the logarithmic decrease observed in both the Schwinger and ANNNI models. Such logarithmic corrections under OBC can arise from boundary effects in the CFT describing the critical point. Similar boundary-induced logarithmic behaviors have been reported for other quantities, such as participation entropies [LLA14] and SREs [HA26]. Determining whether the prefactor a_1 is universal and deriving it analytically would require a more detailed boundary-CFT analysis.

3.3 Real-time meson scattering

After studying the equilibrium phase transition at $\theta = \pi$, we now turn to real-time dynamics in the same LGT model. We employ TDVP, introduced in Section 1.2, to explore elastic and inelastic scattering of composite particles in the lattice Schwinger model. We focus on vanishing background field ($\theta = 0$, equivalently $l = 0$) and in the strong coupling regime, which offers a crucial advantage: it provides a simple ansatz for the initial composite particles involved in the collision and a clear estimate of the momentum threshold for scalar meson production [PKBn25].

At zero background field, the spectrum of the model features two stable particles with well-defined charge conjugation and parity quantum numbers: the lighter vector meson (mass M_v) and the heavier scalar meson (mass M_s). In the scattering setup considered here, the initial state is prepared as two incoming vector meson wave packets with opposite momenta. The simplest possible outcome is then an elastic process, which occurs when the two incoming particles collide with energy below the threshold for production. In this scenario, they scatter without producing additional particles, although the collision can still generate significant entanglement between the outgoing wave packets. By contrast, inelastic scattering requires the particles to carry enough energy to open a new kinematically allowed channel, leading to the production of heavier particles after the collision.

To study this mechanism, we use the spin formulation introduced in Eq. (21) with OBC. As shown in [PKBn25], the first excited state of the theory in the strong-coupling regime, corresponding to the vector meson $|1_V\rangle$, can be approximated by the following ansatz:

$$|1_V\rangle = \frac{1}{\sqrt{N}} \sum_n (\sigma_n^+ \sigma_{n+1}^- - \sigma_{n+1}^+ \sigma_n^-) \, |\Omega\rangle \,, \tag{27}$$

where $|\Omega\rangle$ is the true ground state at finite x. To study the collisions, we prepare the initial state by creating Gaussian superpositions of the operator in Eq. (27) acting on different positions:

$$|\Psi_i\rangle = \mathcal{N}_i \sum_{n=\alpha_i^{\text{beg}}}^{\alpha_i^{\text{end}}} e^{-(n-c_i)^2/(2\sigma^2)} e^{-ink_i} \left(\sigma_n^+ \sigma_{n+1}^- - \sigma_{n+1}^+ \sigma_n^-\right) |\Omega\rangle = \mathcal{O}_i |\Omega\rangle. \tag{28}$$

Here, $i \in \{1, 2\}$ labels the two incoming mesons, c_i is the center of each packet, σ is their spatial width, and k_i is the central momentum. We initialize the first wavepacket on the left half of the chain ($\alpha_1^{\text{beg}} = 0$, $\alpha_1^{\text{end}} = N/2 - 1$) and the second on the right half ($\alpha_2^{\text{beg}} = N/2$, $\alpha_2^{\text{end}} = N - 1$). The two momenta are chosen with equal magnitude and opposite sign, $k_1 = -k_2 = k$. The constants $\mathcal{N}_i$ ensure normalization of each packet. Finally, the total initial state is obtained by applying both operators to the interacting ground state,

$$|\Psi\rangle = (\mathcal{O}_1 \mathcal{O}_2) |\Omega\rangle. \tag{29}$$

For the specific parameters considered in our study, the critical lattice momentum threshold required to satisfy the kinematic constraints for scalar production has been estimated at $k_{\text{thr}} \approx 1.123$ [PKBn25]. Therefore, collisions with $k < k_{\text{thr}}$ are expected to remain

dominantly elastic, while for $k > k_{\rm thr}$ scalar-meson production is allowed. By performing the real-time evolution using TDVP, we will investigate collisions initialized at momenta below and above this threshold.

3.4 Local entropy and antiflatness dynamics

To characterize the products of the collision, we monitor local quantities during the real-time evolution. We first consider a local entanglement entropy corresponding to a bipartition where one subsystem includes two neighboring sites n and $n+1$, and the other subsystem consists of the remaining sites,

$$S(n,t) = -\mathrm{Tr}\left[\rho_{n,n+1}(t)\log_2 \rho_{n,n+1}(t)\right], \tag{30}$$

where $\rho_{n,n+1}$ is the reduced density matrix for the pair of sites $\{n, n+1\}$. This quantity then measures the entanglement between the local two-site subsystem and the rest of the chain. In order to connect this analysis to fermionic non-Gaussianity, we also define a local version of FAF. For a subsystem $A_n = \{n, n+1\}$ containing two neighboring fermionic sites, we restrict the Majorana covariance matrix to the four Majorana modes supported on these sites:

$$(M_{A_n})_{ab} = -\frac{i}{2}\langle\Psi(t)|[\gamma_a,\gamma_b]|\Psi(t)\rangle, \qquad a,b \in \{2n, 2n+1, 2n+2, 2n+3\}. \tag{31}$$

The local FAF is then defined as

$$\mathcal{F}_k(A_n,t) = N_A - \frac{1}{2}\mathrm{Tr}\left[\left(M_{A_n}^T M_{A_n}\right)^k\right], \tag{32}$$

where $N_A = 2$ is the number of fermionic sites in the local subsystem. Therefore, comparing their space-time profiles allows us to distinguish the propagation of the incoming and outgoing mesonic wave packets from the additional correlations generated during the collision.

We now present the results for elastic and inelastic meson-meson scattering in the lattice Schwinger model. We compare collisions with incoming momenta below and above the threshold $k_{\rm thr}$. The simulations are performed at fixed fermion mass $m/g = 10^{-5}$, system size $N = 60$ and inverse lattice spacing $x = 1$. The dimensionless lattice time τ appearing in the evolution operator $|\Psi(\tau)\rangle = e^{-iW\tau}|\Psi(0)\rangle$ is related to the physical time by

$$\tau = \frac{g t_{\rm phys}}{2\sqrt{x}}.$$

The results are shown in Fig. 7 and Fig. 8. To study the opening of the inelastic channel, we examine three different initial momenta: $k = 1.0$, $k = 1.13$, and $k = 1.5$. In the first regime, shown in the left panels of both figures, the momentum is below the production threshold. Here, the incoming vector mesons do not carry sufficient kinetic energy to create new particles. The signal is dominated by two wave packets approaching each other, interacting near the center of the chain, and then emerging with the same magnitude of momentum they had initially. After the collision ($g t_{\rm phys} \gtrsim 50$), the center of the system returns to a state resembling the vacuum, with both the local entropy and FAF dropping back to background levels.

The middle panels illustrate the critical scenario where the incoming momentum is just above the threshold. At this energy, the inelastic channel opens, allowing the system to produce heavier scalar mesons (M_s). However, because the collision energy only marginally

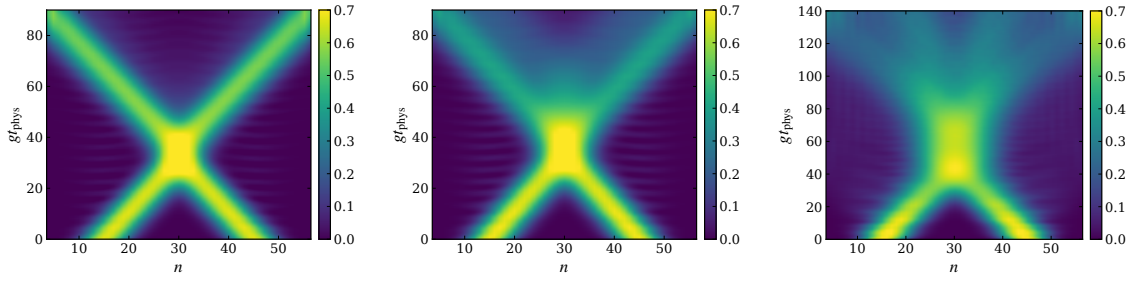

(a) $k = 1.0$ (b) $k = 1.13$ (c) $k = 1.5$

Figure 7: Time evolution of the local entanglement entropy $S(n,t)$ during the collision of two mesonic wave packets for different initial momenta. The three panels correspond to momenta below threshold, close to threshold, and above threshold, respectively. For $k = 1.0$, the wave packets mainly pass through each other while preserving their structure. Near and above the threshold, an enhanced entropy signal develops near the collision region, signaling the additional correlations during the scattering process. All panels show the vacuum-subtracted quantity, computed with Gaussian width $\sigma = 4$ and maximum TDVP bond dimension $\chi = 50$.

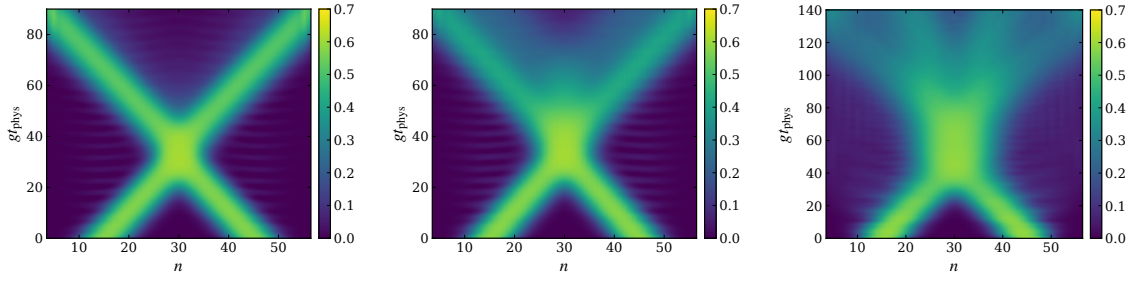

(a) $k = 1.0$ (b) $k = 1.13$ (c) $k = 1.5$

Figure 8: Time evolution of the local FAF during the collision of two mesonic wave packets for different initial momenta. For momenta below the threshold, local FAF mainly follows the propagation of the incoming wave packets, consistent with an elastic scattering process. Near and above the threshold, a strong increase of FAF is observed in the collision region, signaling the generation of non-Gaussian correlations and particle production. All panels show the vacuum-subtracted quantity, computed with Gaussian width $\sigma = 4$ and maximum TDVP bond dimension $\chi = 50$.

exceeds the mass threshold, the newly created particles are produced with almost zero velocity. This phenomenon is captured well by our complexity markers. For $gt_{\mathrm{phys}} \gtrsim 50$, a persistent vertical signal emerges in the central region of the lattice. This central peak in the local entropy and FAF marks the presence of the newly produced, slow-moving scalar mesons. The higher peaks on the left and right of this signal correspond to the outgoing mesons of the elastic channel.

Finally, the right panels correspond to the deep inelastic regime. In this case, the incoming mesons carry enough energy to transfer significant kinetic energy to the newly produced particles. As a result, both channels are distinguishable. The elastic channel is present near the edges of the plot, while the inelastic contribution appears as a slower signal inside the main outgoing light cone. The comparison between the entropy and FAF profiles suggests that the local FAF provides a complementary diagnostic of the collision process. Overall, the local FAF clearly distinguishes the elastic and inelastic regimes. While below the threshold it mainly follows the propagation of the original wave packets, above the threshold it develops a strong signal in the collision region, consistent with the generation of non-Gaussian correlations associated with particle production.

4 Conclusions

This work has investigated fermionic non-Gaussianity as a diagnostic of quantum many-body complexity in systems motivated by high-energy physics. The main quantity used throughout the thesis has been the FAF, which quantifies the deviation of a fermionic state from Gaussianity, and provides information that is complementary to the entanglement entropy.

The first part studied a Hamiltonian interpolating between the chaotic SYK_4 model and an integrable transverse-field Ising chain. In the ground state, both entanglement entropy and FAF decrease when moving from the chaotic SYK_4 regime toward the integrable Ising regime. The Ising limit provides a useful benchmark because it is quadratic in fermionic variables, so its eigenstates are fermionic Gaussian and the FAF vanishes. However, the behavior of FAF is not only controlled by the interpolation parameter λ, but also presents a strong dependence on the system size and symmetry class, especially in the pure SYK_4 limit. Therefore, FAF is sensitive not only to chaos/integrability, but also to the RMT symmetry class of the Hamiltonian, leading to anomalous values of FAF for $N \equiv 0 \pmod 4$. In the middle of the spectrum, the average FAF approaches the Haar-random prediction as N increases, consistent with the expected typical-state behavior of highly excited eigenstates in ergodic systems. Nevertheless, the approach to this typical value retains a clear N mod 4 dependence. Overall, the SYK_4-Ising analysis shows that FAF is a sensitive probe of fermionic complexity, but also that its interpretation requires careful control of the symmetry class and finite-size effects.

The second part applied FAF to the lattice Schwinger model, a gauge theory relevant as a benchmark for non-perturbative physics. The model was studied at $\theta = \pi$, where it undergoes a CP-symmetry-breaking quantum phase transition belonging to the Ising universality class. In this case, FAF and entanglement entropy show an enhancement close to the critical region, confirming that both complexity markers are sensitive to the increase of correlations near the phase transition. By studying the dependence of FAF on the system size, one can analyze the subleading contribution, which contains the most relevant information about criticality. These results suggest that FAF can be used not only as a general complexity marker, but also as a diagnostic of phase transitions in a LGT.

The final part studied out-of-equilibrium dynamics in the Schwinger model through the collision of two fermionic wave packets. This part was motivated by the difficulty of simulating real-time scattering processes in non-perturbative gauge theories. Local observables such as the local entropy and local FAF were used to monitor the spatial and temporal structure of the collision. Below the threshold, the wave packets mainly pass through each other while preserving their structure, while near and above the threshold, a stronger FAF signal appears in the collision region, consistent with the onset of particle production. All in all, the scattering results show that local FAF can resolve qualitative changes in real-time dynamics and provides a useful probe of non-Gaussian correlations generated during inelastic scattering.

Across all three applications, FAF behaves as a meaningful marker of fermionic complexity. These results support the idea that fermionic non-Gaussianity is a useful notion of complexity for many-body systems, complementary to entanglement and stabilizer-based measures. Moreover, a key advantage of FAF is that it is built from Majorana two-point correlation functions, making it computationally accessible with both ED and TN techniques.

Several limitations of the present work also point toward natural directions for future research. As discussed in the analysis of the middle-spectrum SYK_4 eigenstates, our results

are limited to relatively small system sizes. Consequently, although the data are consistent with a suppression of the finite-size corrections, they do not allow for a reliable statistical extraction of the exponent β. A more complete characterization of FAF across the different N mod 4 symmetry classes would require larger system sizes and a larger number of disorder realizations.

Beyond the SYK analysis, the phase-transition data are obtained at finite lattice spacing, so a full continuum extrapolation remains necessary. Moreover, it would be interesting to perform a complete universality study of the FAF in the Schwinger model and determine whether the subleading logarithmic prefactor is a universal quantity, as well as whether it can be derived analytically from the underlying critical theory.

Bibliography

[ACTX25] Erick Arguello Cruz, Grigory Tarnopolsky, and Yuan Xin. Precision study of the massive schwinger model near quantum criticality. *Phys. Rev. D*, 112:034023, Aug 2025.

[AFOV08] Luigi Amico, Rosario Fazio, Andreas Osterloh, and Vlatko Vedral. Entanglement in many-body systems. *Rev. Mod. Phys.*, 80:517–576, May 2008.

[BSBH02] T. M. R. Byrnes, P. Sriganesh, R. J. Bursill, and C. J. Hamer. Density matrix renormalization group approach to the massive schwinger model. *Physical Review D*, 66(1), July 2002.

[BSK76] T. Banks, Leonard Susskind, and John Kogut. Strong-coupling calculations of lattice gauge theories: (1 + 1)-dimensional exercises. *Phys. Rev. D*, 13:1043–1053, Feb 1976.

[BSS16] Sergey Bravyi, Graeme Smith, and John A. Smolin. Trading classical and quantum computational resources. *Phys. Rev. X*, 6:021043, Jun 2016.

[CCJ+25] Yahui Chai, Arianna Crippa, Karl Jansen, Stefan Kühn, Vincent R. Pascuzzi, Francesco Tacchino, and Ivano Tavernelli. Fermionic wave packet scattering: a quantum computing approach. *Quantum*, 9:1638, February 2025.

[CGAH+17] Jordan S. Cotler, Guy Gur-Ari, Masanori Hanada, Joseph Polchinski, Phil Saad, Stephen H. Shenker, Douglas Stanford, Alexandre Streicher, and Masaki Tezuka. Black holes and random matrices. *Journal of High Energy Physics*, 2017(5), may 2017.

[DHK24] Zohreh Davoudi, Chung-Chun Hsieh, and Saurabh V. Kadam. Scattering wave packets of hadrons in gauge theories: Preparation on a quantum computer. *Quantum*, 8:1520, November 2024.

[ECP10] J. Eisert, M. Cramer, and M. B. Plenio. Colloquium: Area laws for the entanglement entropy. *Rev. Mod. Phys.*, 82:277–306, Feb 2010.

[FBFT25] Gerald E. Fux, Benjamin Béri, Rosario Fazio, and Emanuele Tirrito. Disentangling magic states with classically simulable quantum circuits. *Phys. Rev. Lett.*, 135:260605, Dec 2025.

[GGV16] Antonio M. García-García and Jacobus J.M. Verbaarschot. Spectral and thermodynamic properties of the sachdev-ye-kitaev model. *Physical Review D*, 94(12), dec 2016.

[HA26] Masahiro Hoshino and Yuto Ashida. Stabilizer rényi entropy encodes fusion rules of topological defects and boundaries. *Phys. Rev. Lett.*, 136:080402, Feb 2026.

[HCO+11] Jutho Haegeman, J. Ignacio Cirac, Tobias J. Osborne, Iztok Pižorn, Henri Verschelde, and Frank Verstraete. Time-dependent variational principle for quantum lattices. *Phys. Rev. Lett.*, 107:070601, Aug 2011.

[JW28] P. Jordan and E. Wigner. Über das paulische Äquivalenzverbot. *Zeitschrift für Physik*, 47(9):631–651, 1928.

[KS75] John Kogut and Leonard Susskind. Hamiltonian formulation of wilson's lattice gauge theories. *Phys. Rev. D*, 11:395–408, Jan 1975.

[LLA14] David J Luitz, Nicolas Laflorencie, and Fabien Alet. Participation spectroscopy and entanglement hamiltonian of quantum spin models. *Journal of Statistical Mechanics: Theory and Experiment*, 2014(8):P08007, Aug 2014.

[LLXZ17] Tianlin Li, Junyu Liu, Yuan Xin, and Yehao Zhou. Supersymmetric syk model and random matrix theory. *Journal of High Energy Physics*, 2017(6), jun 2017.

[LOH22] Lorenzo Leone, Salvatore F. E. Oliviero, and Alioscia Hamma. Stabilizer rényi entropy. *Phys. Rev. Lett.*, 128:050402, Feb 2022.

[LRV04] J. I. Latorre, E. Rico, and G. Vidal. Ground state entanglement in quantum spin chains, 2004.

[Oha23] Hiroki Ohata. Phase diagram near the quantum critical point in schwinger model at $\theta = \pi$: analogy with quantum ising chain, 2023.

[PDR+16] T. Pichler, M. Dalmonte, E. Rico, P. Zoller, and S. Montangero. Real-time dynamics in u(1) lattice gauge theories with tensor networks. *Physical Review X*, 6(1), Mar 2016.

[PKBn25] Irene Papaefstathiou, Johannes Knolle, and Mari Carmen Bañuls. Real-time scattering in the lattice schwinger model. *Phys. Rev. D*, 111:014504, Jan 2025.

[Sac15] Subir Sachdev. Bekenstein-hawking entropy and strange metals. *Phys. Rev. X*, 5:041025, Nov 2015.

[Sch11] Ulrich Schollwöck. The density-matrix renormalization group in the age of matrix product states. *Annals of Physics*, 326(1):96–192, Jan 2011.

[SCS25] Haiyang Shao, Shile Chen, and Shuzhe Shi. Collective motion in the massive schwinger model via tensor network, 2025.

[Sre94] Mark Srednicki. Chaos and quantum thermalization. *Phys. Rev. E*, 50:888–901, Aug 1994.

[SST26] Piotr Sierant, Paolo Stornati, and Xhek Turkeshi. Fermionic magic resources of quantum many-body systems. *PRX Quantum*, 7(1), jan 2026.

[Sto22] Paolo Stornati. *Variational Quantum Simulations of Lattice Gauge Theories*. PhD thesis, Humboldt U., Berlin, 2022.

[SWB+25] Gopal Chandra Santra, Alex Windey, Soumik Bandyopadhyay, Andrea Legramandi, and Philipp Hauke. Complexity transitions in chaotic quantum systems: Nonstabilizerness, entanglement, and fractal dimension in syk and random matrix models, 2025.

[Val01] Leslie G. Valiant. Quantum computers that can be simulated classically in polynomial time. In *Proceedings of the Thirty-Third Annual ACM Symposium on Theory of Computing*, STOC '01, page 114–123, New York, NY, USA, 2001. Association for Computing Machinery.

[Vid03] Guifré Vidal. Efficient classical simulation of slightly entangled quantum computations. *Phys. Rev. Lett.*, 91:147902, Oct 2003.

[VLRK03] G. Vidal, J. I. Latorre, E. Rico, and A. Kitaev. Entanglement in quantum critical phenomena. *Physical Review Letters*, 90(22), June 2003.

[VMGE14] Victor Veitch, S. A. Hamed Mousavian, Daniel Gottesman, and Joseph Emerson. The resource theory of stabilizer quantum computation. *New Journal of Physics*, 16(1):013009, 2014.

[Whi92] Steven R. White. Density matrix formulation for quantum renormalization groups. *Phys. Rev. Lett.*, 69:2863–2866, Nov 1992.

[Wil74] Kenneth G. Wilson. Confinement of quarks. *Phys. Rev. D*, 10:2445–2459, Oct 1974.

[Wit98] Edward Witten. Anti de sitter space and holography, 1998.

[WSL04] L.-A. Wu, M. S. Sarandy, and D. A. Lidar. Quantum phase transitions and bipartite entanglement. *Phys. Rev. Lett.*, 93:250404, Dec 2004.

A Disorder Realizations

In order to mitigate the effects of statistical fluctuations arising from the random couplings $J_{i_1 \cdots i_4}$ in the SYK_4 contribution, the physical observables are averaged over an ensemble of disorder realizations. For numerical reproducibility, we provide in Table 1 the exact number of disorder realizations computed for each system size N for the ground state. Because the Hilbert space dimension grows exponentially with N, we scale down the number of realizations with increasing N to keep the numerical effort manageable. However, this reduction is partially compensated by the increasing self-averaging of the observables [SWB+25].

System Size (N)	**Number of Realizations**
$8, 9, 10$	100
$11, 12$	40
$13, 14$	15
$15, 16$	5

Table 1: Number of disorder realizations computed for the ensemble averaging as a function of the system size N (number of qubits) for the ground state properties.

For the excited-state analysis, including both the FAF across the full energy spectrum and the average over middle-spectrum eigenstates, we use the number of disorder realizations reported in Table 2.

System Size (N)	**Number of Realizations**
$5, 6, 7$	1000
$8, 9$	100
$10, 11$	40
$12, 13$	10
$14, 15$	4
16	1

Table 2: Number of disorder realizations used for the full-spectrum and middle-spectrum eigenstate analyses as a function of the system size N.

B Dependence of FAF on k

In Fig. 9, we present the FAF $\mathcal{F}_k$ for $k = 1, 2$ to confirm that they exhibit the same qualitative behavior.

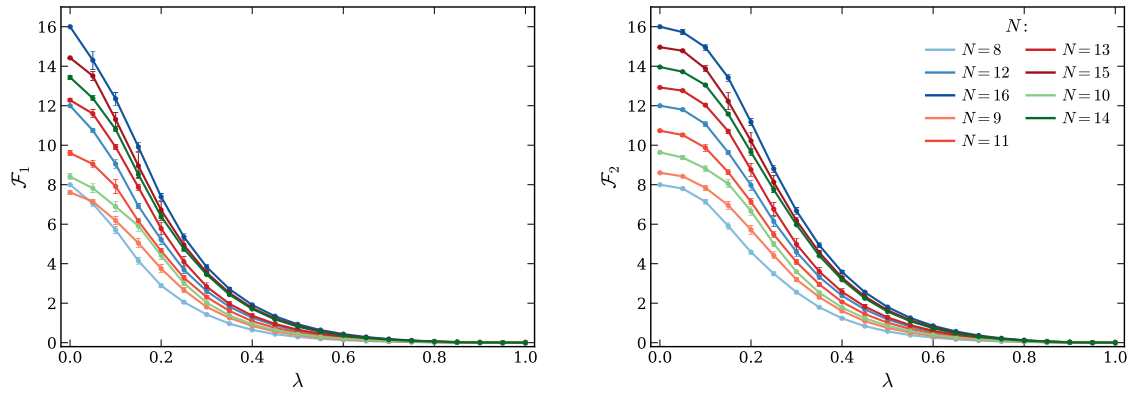

Figure 9: Disorder-averaged FAF $\mathcal{F}_1$ and $\mathcal{F}_2$ as a function of the interpolation parameter λ for the ground state of the Hamiltonian in Eq. (8).